J. Fluid Mech. (1991), *vol.* 226, *pp.* 401–423
Printed in Great Britain

On the interaction of a collapsing cavity and a compliant wall

By J. H. DUNCAN AND S. ZHANG
Department of Mechanical Engineering, University of Maryland, College Park, MD 20742, USA

(Received 8 June 1990 and in revised form 5 November 1990)

The collapse of a spherical vapour cavity in the vicinity of a compliant boundary is examined numerically. The fluid is treated as a potential flow and a boundary-element method is used to solve Laplace's equation for the velocity potential. Full nonlinear boundary conditions are applied on the surface of the cavity. The compliant wall is modelled as a membrane with a spring foundation. At the interface between the fluid and the membrane, the pressure and vertical velocity in the flow are matched to the pressure and vertical velocity of the membrane using linearized conditions. The results of calculations are presented which show the effect of the parameters describing the flow (the initial cavity size and position, the fluid density and the pressure driving the collapse) and the parameters describing the compliant wall (the mass per unit area, membrane tension, spring constant and coating radius) on the interaction between the two. When the wall is rigid, the collapse of the cavity is characterized by the formation of a re-entrant jet that is directed toward the wall. However, if the properties of the compliant wall are chosen properly, the collapse can be made to occur spherically, as if the cavity were in an infinite fluid, or with the re-entrant jet directed away from the wall, as if the cavity were adjacent to a free surface. This behaviour is in qualitative agreement with the experiments of Gibson & Blake (1982) and Shima, *et al.* (1989). Calculations of the transfer of energy between the flow and the coating are also presented.

1. Introduction

The growth and collapse of vapour cavities in the vicinity of plane boundaries has been the subject of a number of theoretical, numerical and experimental investigations (see the review article by Blake & Gibson 1987). When the boundary is a rigid wall, the collapse is characterized by the formation of a re-entrant jet that is directed toward the wall (Plesset & Chapman 1970; Chahine & Bovis 1983; Blake, Taib & Doherty 1986; Vogel, Lauterborn & Timm 1989). In a recent experimental investigation, Tomita & Shima (1986) found that the erosion of wall material during the collapse was related to the behaviour of this re-entrant jet. When the plane boundary is a free surface, a re-entrant jet is also formed. However, in this case, the jet is directed away from the free surface (Chahine 1977; Blake & Gibson 1981; Dommermuth & Yue 1987).

The laboratory investigations of Rheingans (1950) and Lichtman (1967) have indicated that surfaces coated with elastomeric materials are more resistant to cavitation erosion. Theorizing that this increased resistance to erosion might result from a redirection of the re-entrant jet in a manner similar to a free surface, Gibson & Blake (1982) photographed the collapse of spark-generated cavities in the vicinity of walls covered by elastomeric coatings of several compositions. They found that under some circumstances the collapse was modified such that a jet was indeed directed away from the wall. To identify coating properties that would produce this redirection of the jet, they devised a simple non-interactive model. First, using data from the calculation of the collapse of a spherical cavity in an infinite fluid, they computed the average pressure force and average displacement in the fluid on an imaginary surface at the position where the wall would be located in the interactive case. Then, using a one-dimensional spring-mass-damper model of the coating, they found coating designs whose impedance matched the average force and average displacement characteristics in the spherical collapse. In this way, they attempted to find the coating properties that would make the collapse spherical when the cavity was adjacent to the compliant wall. It was theorized that further softening of the wall properties would result in a re-entrant jet that was directed away from the wall. This analysis indicated a tentative beneficial parameter range for the coatings. A more detailed set of experiments with spark-generated bubbles adjacent to a compliant surface has been reported by Shima *et al.* (1989). The compliant surface consisted of a thin layer of rubber backed by a layer of foam. The position and size of the cavity and the thickness of the rubber and foam layers were varied. The shape of the cavity was measured photographically. The results showed again that it is possible to redirect the re-entrant jet away from the wall with a properly designed compliant coating and gave detailed information on the history of the cavity shape. No measurements of the motion of the compliant surface were reported.

The computational methods for the collapse of a cavity in the vicinity of a rigid wall (e.g. Blake *et al.* 1986) and a free surface (e.g. Blake, Taib & Doherty 1987) are well developed. In these methods, the fluid motion is assumed to be inviscid and incompressible and the fluid velocity is obtained from the gradient of a scalar Eulerian velocity potential which satisfies Laplace's equation. Fluid particles on the free surfaces are tracked in time and Bernoulli's equation is used to obtain the velocity potential at the position of these particles. At each time step, an integral equation is solved to obtain the value of the fluid velocity in the direction normal to the surfaces. The rigid surface is usually simulated with an image cavity.

In the present paper, the collapse of a cavity near a compliant wall is explored numerically. In particular, the above-mentioned potential flow model for the fluid motion has been coupled to a rigid wall with a central region containing a compliant coating modelled as a spring-backed membrane. This coating is characterized by its mass per unit area (m), membrane tension (T), spring stiffness per unit area (K) and radius (R_m). The coating is coupled to the flow model through the normal velocity and the pressure at the flow–coating interface. Linearized boundary conditions are applied at the location of the undisturbed membrane surface. A detailed account of the theory behind this fully interactive model is given in §2 and its numerical implementation is described in §3. Calculations are presented in §4 which show the effect of the coating and cavity characteristics on the collapse. It is also noted in §4 that this model is not a good representation of the experiments of Shima *et al.* (1989). However, some comparisons with their data are included which show qualitative agreement. The conclusions of the work are given in §5.

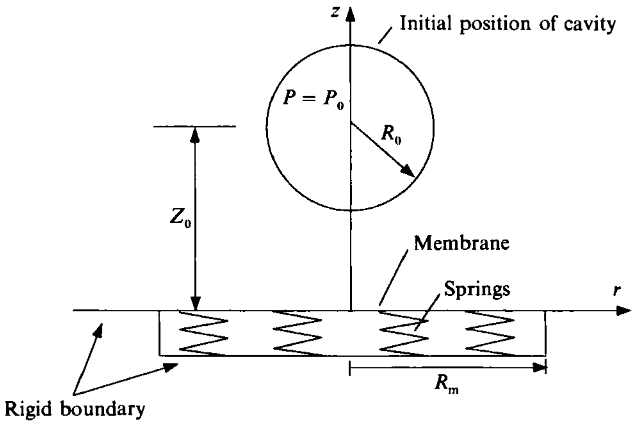

FIGURE 1. Schematic showing the coordinate system and the initial position of the cavity and the compliant boundary.

2. Mathematical formulation

A schematic showing the initial position of the cavity, the wall and the coordinate system used in the calculations is given in figure 1. The coordinate system is cylindrical with the z-axis piercing the centre of the cavity and directed normal to the undisturbed surface of the wall which is located at $z = 0$. The radial coordinate is r and the circumferential angle is θ. The compliant surface is centred at $r = 0$ and has a radius R_m; outside this region the wall is rigid. The problem is axisymmetric about the z-axis. The cavity is initially ($t = 0$) spherical with radius R_0, its maximum value, and its centre is located at $z = Z_0$. For times before the initial instant, the pressure everywhere in the fluid and inside the cavity is P_∞. At $t = 0$, the pressure in the cavity is reduced to P_0 and is held constant at this value for the entire collapse. The pressure in the fluid far from the cavity is maintained constant at P_∞. The theoretical model for the fluid is similar to the one used by a number of investigators including, most recently, Blake *et al.* (1986). The fluid motion is assumed to be incompressible and inviscid and therefore satisfies Laplace's equation:

$$\nabla^2\phi = 0, \tag{1}$$

where $\boldsymbol{\nabla}$ is the gradient operator and ϕ is the velocity potential. The fluid velocity is equal to the gradient of the velocity potential, $\boldsymbol{u} = \boldsymbol{\nabla}\phi$. On the surface of the cavity, the pressure in the fluid is equal to the pressure in the cavity, P_0. The condition imposed on ϕ by this dynamic boundary condition can be written as Bernoulli's equation in material derivative form:

$$\frac{\mathrm{D}\phi}{\mathrm{D}t} = \tfrac{1}{2}|\boldsymbol{\nabla}\phi|^2 + \frac{P_\infty - P_0}{\rho}, \tag{2}$$

where $\mathrm{D}/\mathrm{D}t$ is the derivative with respect to time following a fluid particle. The kinematic boundary condition on the surface of the cavity states that material points remain on the surface of the cavity:

$$\frac{\mathrm{D}\boldsymbol{x}_c}{\mathrm{D}t} = \boldsymbol{\nabla}\phi, \tag{3}$$

where $\boldsymbol{x}_c$ is the position vector to these material points.

For $r < R_m$, the wall is modelled as a spring-backed membrane with mass per unit area m, spring constant K and tension T. For $r > R_m$, the wall is rigid. The equation describing the motion of the compliant section of the wall is

$$m\frac{\partial^2\eta}{\partial t^2}-T\frac{1}{r}\frac{\partial}{\partial r}\left(r\frac{\partial\eta}{\partial r}\right)+K\eta=-(P_m(r,t)-P_\infty), \tag{4}$$

where $\eta=\eta(r,t)$ is the vertical displacement of the membrane surface and P_m is the pressure on the membrane surface. For $t<0$, the springs are compressed uniformly owing to the steady, uniform pressure, P_∞, applied by the fluid. The displacement of the membrane at this time is taken as zero. The membrane is assumed to be attached to the rigid boundary at $r=R_m$ so the vertical displacements at this point are taken as zero, $\eta(R_m,t)=0$. During the collapse, the fluid and the membrane are coupled using linearized equations for the pressure and velocity in the two systems. These equations are satisfied at the undisturbed position of the coating surface $z=0$:

$$\frac{\partial\eta}{\partial t}=w(r,0,t)=\frac{\partial\phi}{\partial z}, \tag{5}$$

$$P_m(r,t)=P(r,0,t)=-\rho\frac{\partial\phi}{\partial t}+P_\infty, \tag{6}$$

where the last equation is the linearized Bernoulli equation.

To show how the system of equations can be advanced in time, let us assume that at time t_i all dependent variables are known. The boundary conditions on the surface of the cavity, equations (2) and (3), are integrated numerically to get the position of the surface of the cavity and the value of ϕ on the cavity at time t_{i+1}. The membrane equation can be used to obtain the value of $\partial\eta/\partial t=-\partial\phi/\partial n$ on the membrane surface at t_{i+1}. On the rigid part of the wall, $\partial\phi/\partial n=0$. In order to move on to the next time step, t_{i+2}, the values of $\nabla\phi$ must be known on the cavity surface for use in (2) and (3). However, at this point only the value of $\partial\phi/\partial s$ can be computed (where s is a coordinate along the cavity surface). Also, in order to find the value of $\partial\phi/\partial n$ on the membrane surface at t_{i+2}, the pressure must be known on the membrane surface at t_{i+1} for use in (4). The pressure at t_{i+1} can be obtained from Bernoulli's equation if $\partial\phi/\partial t$ is known, (6). Thus, the value of ϕ on the membrane at time t_{i+1} must be found to obtain a finite-difference approximation for $\partial\phi/\partial t$. To complete the problem, the values of $\partial\phi/\partial n$ on the cavity surface and ϕ on the membrane surface are obtained by solving Laplace's equation in the form of an integral equation (Lamb 1945):

$$\int_{S_c+S_w} g(\boldsymbol{p},\boldsymbol{q})\frac{\partial\phi}{\partial n}\,\mathrm{d}S_q-\int_{S_c+S_w}\frac{\partial g(\boldsymbol{p},\boldsymbol{q})}{\partial n}\phi(\boldsymbol{q})\,\mathrm{d}S_q=2\pi\phi(\boldsymbol{p}), \tag{7}$$

where S_c is the surface of the cavity, S_w is the interface between the wall and the fluid, $\boldsymbol{p}$ is a field point that is on the surface $S=S_c+S_w$, $\boldsymbol{q}$ is a source point that is also on S, $g(\boldsymbol{p},\boldsymbol{q})=1/|\boldsymbol{p}-\boldsymbol{q}|$, n is the normal to S directed outward from the fluid and $\mathrm{d}S_q$ is the area element of S varying the point $\boldsymbol{q}$. Since the problem is axisymmetric, the positions of the field points need only be considered in a single plane, $\theta=0$. Once this equation is solved, the calculation can proceed on to the next time step or, with a companion form of this integral equation, the velocity and pressure can be found at any point in the fluid.

The computation of the energy of the flow and the coating is useful for interpreting the physics of the phenomenon. The integral energy equation for the flow is obtained by integrating the mechanical energy equation

$$\frac{\partial \frac{1}{2}q^2}{\partial t}+\nabla\cdot\left[\left(\tfrac{1}{2}q^2+\frac{P}{\rho}\right)\boldsymbol{u}\right]=0 \tag{8}$$

over a volume bounded by the surface of the cavity (S_c), a hemispherical material surface (S_h) centred on $(r,z)=(0,0)$ with a large but finite radius, and the surface of the wall ($S_w=S_m+S_r$, where S_m is the membrane surface and S_r is the surface of the rigid wall). After performing the integrations and using the divergence theorem and the transport theorem, this equation can be written:

$$\frac{\mathrm{d}}{\mathrm{d}t}\int_{V_f}\tfrac{1}{2}q^2\,\mathrm{d}V+\int_{S_c}\boldsymbol{u}\cdot\hat{\boldsymbol{n}}\frac{P_0}{\rho}\mathrm{d}S+\int_{S_m}\boldsymbol{u}\cdot\hat{\boldsymbol{n}}\frac{P_m}{\rho}\mathrm{d}S+\int_{S_h}\boldsymbol{u}\cdot\hat{\boldsymbol{n}}\frac{P_h}{\rho}\mathrm{d}S=0, \tag{9}$$

where q is the magnitude of the fluid velocity, V_f is the total volume inside the surfaces, the P are the pressures on the surfaces denoted by the subscripts, $\hat{\boldsymbol{n}}$ is the outward unit normal to the surfaces and the condition $\boldsymbol{u}\cdot\hat{\boldsymbol{n}}=0$ has been used on the rigid part of the wall. The pressure on the surface of the cavity has been taken as P_0. When the radius of the hemispherical surface becomes large, the pressure P_h approaches P_∞. In this case, the conservation of mass in integral form,

$$\int_{S_c}\boldsymbol{u}\cdot\hat{\boldsymbol{n}}\,\mathrm{d}S+\int_{S_m}\boldsymbol{u}\cdot\hat{\boldsymbol{n}}\,\mathrm{d}S+\int_{S_h}\boldsymbol{u}\cdot\hat{\boldsymbol{n}}\,\mathrm{d}S=0, \tag{10}$$

can be used to eliminate the integral over the hemisphere. Thus, the energy equation can be written

$$\frac{\mathrm{d}}{\mathrm{d}t}\int_{V_f}\tfrac{1}{2}q^2\,\mathrm{d}V+\frac{P_0-P_\infty}{\rho}\int_{S_c}\boldsymbol{u}\cdot\hat{\boldsymbol{n}}\,\mathrm{d}S+\int_{S_m}\frac{P_m-P_\infty}{\rho}\boldsymbol{u}\cdot\hat{\boldsymbol{n}}\,\mathrm{d}S=0. \tag{11}$$

Finally, this equation is integrated in time to yield

$$\int_{V_f}\tfrac{1}{2}q^2\,\mathrm{d}V+\frac{P_\infty-P_0}{\rho}V_c(t)+\int_0^t\int_{S_m}\frac{P_m-P_\infty}{\rho}\boldsymbol{u}\cdot\hat{\boldsymbol{n}}\,\mathrm{d}S\,\mathrm{d}t=\frac{P_\infty-P_0}{\rho}V_c(0), \tag{12}$$

where V_c is the volume of the cavity. The first term on the left-hand side is the kinetic energy of the fluid (KEF) and can be obtained from surface integrals over the cavity and the wall:

$$\int_{V_f}\tfrac{1}{2}q^2\,\mathrm{d}V=\frac{1}{2}\int_{S_c+S_w}\phi\frac{\partial\phi}{\partial n}\mathrm{d}s \tag{13}$$

(Lamb 1945). The second term on the left-hand side of (12) is the potential energy (PEF) associated with work against the pressure at infinity as the volume of the cavity changes. The third term on the left-hand side is the pressure work term at the flow-membrane boundary (PW). In the following, this term is evaluated at $z=0$. The pressure work term represents the transfer of energy between the flow and the coating. The sum of these three terms equals the initial potential energy which appears on the right-hand side.

The energy equation for the coating is obtained by multiplying the membrane equation by the membrane velocity and integrating over the surface of the membrane. Thus, one obtains

$$m\int_0^{R_\mathrm{m}}\left(\frac{\partial\eta}{\partial t}\right)^2\pi r\,\mathrm{d}r+T\int_0^{R_\mathrm{m}}\left(\frac{\partial\eta}{\partial r}\right)^2\pi r\,\mathrm{d}r+K\int_0^{R_\mathrm{m}}\eta^2\pi r\,\mathrm{d}r$$
$$=-\int_0^t\int_0^{R_\mathrm{m}}(P_\mathrm{m}-P_\infty)\frac{\partial\eta}{\partial t}2\pi r\,\mathrm{d}r\,\mathrm{d}t. \tag{14}$$

The first term on the left-hand side is the kinetic energy of the membrane (KEM). The next two terms are the potential energies in the tension (PET) and the spring backing (PES). The right-hand side is the pressure work. It is identical to the pressure work in the fluid energy equation (12) when it is applied at $z = 0$ and the kinematic boundary condition (5) is used.

3. Numerical implementation

In the numerical model, the surface of the cavity is approximated by a set of panels each of which is obtained by rotating a straight line in the $\theta = 0$ plane about the z-axis (see figure 2). The cavity is composed of n_c of these panels. The flat interface between the fluid and the wall at $z = 0$ is modelled by a set of n_w panels consisting of n_m membrane panels with equal length and $n_\mathrm{w}-n_\mathrm{m}$ rigid wall panels with non-equal length. Field points (nodes) are taken at the positions where the line of intersection of two adjacent panels pierces the $\theta = 0$ plane. A predictor-corrector scheme sometimes referred to as Heun's method (see Ferziger 1981) is used to integrate the boundary conditions on the cavity and the membrane equation in time. The r- and z-coordinates of the nodes on the cavity and the corresponding values of ϕ at t_{i+1} are expressed in a vector form as:

Predictor step:

$$\begin{Bmatrix}\bar{r}^j_{i+1}\\ \bar{z}^j_{i+1}\\ \bar{\phi}^j_{i+1}\end{Bmatrix}=\begin{Bmatrix}r^j_i\\ z^j_i\\ \phi^j_i\end{Bmatrix}+(t_{i+1}-t_i)\begin{Bmatrix}u^j_i\\ w^j_i\\ \frac{1}{2}|\nabla\phi^j_i|^2+\dfrac{P_\infty-P_0}{\rho}\end{Bmatrix}, \tag{15}$$

Corrector step:

$$\begin{Bmatrix}r^j_{i+1}\\ z^j_{i+1}\\ \phi^j_{i+1}\end{Bmatrix}=\begin{Bmatrix}r^j_i\\ z^j_i\\ \phi^j_i\end{Bmatrix}+\tfrac{1}{2}(t_{i+1}-t_i)\begin{Bmatrix}u^j_i+\bar{u}^j_{i+1}\\ w^j_i+\bar{w}^j_{i+1}\\ \frac{1}{2}|\nabla\phi^j_i|^2+\frac{1}{2}|\nabla\bar{\phi}^j_{i+1}|^2+2\dfrac{P_\infty-P_0}{\rho}\end{Bmatrix}, \tag{16}$$

where the superscript refers to the nodes and the subscript refers to the time step. The value of $|\nabla\phi|$ is computed from the derivative of ϕ in the direction normal to the cavity surface, which is obtained from the solution of the integral equation, and the derivative in the direction tangent to the surface, which is obtained from a central-difference scheme.

The membrane equation (4) is decomposed into two first-order differential equations with respect to time:

$$\frac{\partial\eta}{\partial t}=\xi, \tag{17}$$

$$\frac{\partial\xi}{\partial t}=\frac{T}{m}\frac{1}{r}\frac{\partial}{\partial r}\left(r\frac{\partial\eta}{\partial r}\right)-\frac{K}{m}\eta-\frac{P_\mathrm{m}(r,t)-P_\infty}{m}. \tag{18}$$

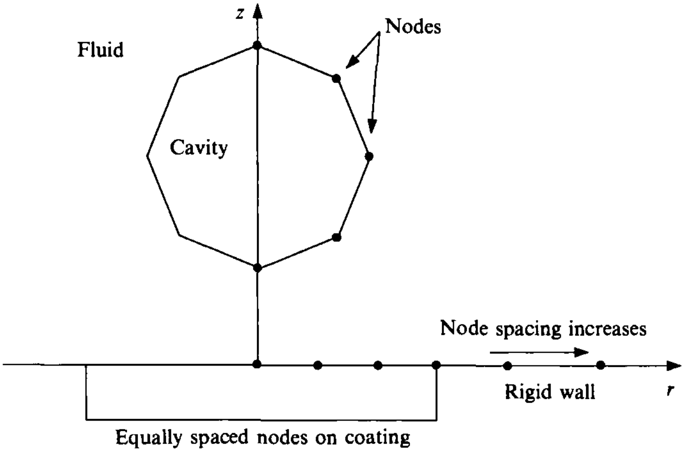

FIGURE 2. Nodes and panels on the surface of the cavity and the flow–wall interface.

The application of the predictor-corrector scheme to these equations yields:
Predictor step:

$$\begin{Bmatrix} \bar{\eta}_{i+1}^j \\ \bar{\xi}_{i+1}^j \end{Bmatrix} = \begin{Bmatrix} \eta_i^j \\ \xi_i^j \end{Bmatrix} + (t_{i+1}-t_i) \begin{Bmatrix} \xi_i^j \\ \left[\dfrac{\partial \xi}{\partial t}\right]_i^j \end{Bmatrix}, \tag{19}$$

Corrector step:

$$\begin{Bmatrix} \eta_{i+1}^j \\ \xi_{i+1}^j \end{Bmatrix} = \begin{Bmatrix} \eta_i^j \\ \xi_i^j \end{Bmatrix} + \tfrac{1}{2}(t_{i+1}-t_i) \begin{Bmatrix} \xi_i^j + \bar{\xi}_{i+1}^j \\ \left[\dfrac{\partial \xi}{\partial t}\right]_i^j + \left[\dfrac{\partial \xi}{\partial t}\right]_{i+1}^j \end{Bmatrix}, \tag{20}$$

where

$$\left[\frac{\partial \xi}{\partial t}\right]_i^j = \frac{T}{m}\left[\frac{1}{r}\frac{\partial}{\partial r} r \frac{\partial \eta}{\partial r}\right]_i^j - \frac{K}{m}\eta_i^j - \frac{P_{\mathrm{m}}(r_j, t_i) - P_\infty}{m}$$

and

$$\left[\frac{1}{r}\frac{\partial}{\partial r} r \frac{\partial \eta}{\partial r}\right]_i^j = \begin{cases} \left(\dfrac{1}{\Delta r^2} + \dfrac{1}{2\Delta r r^j}\right)\eta_i^{j+1} - \dfrac{2}{\Delta r^2}\eta_i^j + \left(\dfrac{1}{\Delta r^2} - \dfrac{1}{2\Delta r r^j}\right)\eta_i^{j-1} & (0 < r^j < R_{\mathrm{m}}), \\ \dfrac{4}{\Delta r^2}(\eta_i^{j+1} - \eta_i^j) & (r^j = 0). \end{cases}$$

In the above equation, Δr is the radial distance between nodes on the membrane and the boundary conditions $\partial \eta / \partial r = 0$ at $r = 0$ and $\eta = 0$ at $r = R_{\mathrm{m}}$ have been used. The former boundary condition is a consequence of symmetry, while the latter boundary condition is a consequence of the attachment of the membrane to the rigid boundary at $r = R_{\mathrm{m}}$. The reflected waves that are introduced by this attachment are caused by physical processes rather than numerical inaccuracies.

The numerical forms of the boundary conditions at the flow–membrane interface, (5) and (6), are

$$\left[\frac{\partial \eta}{\partial t}\right]_i^j = \left[\frac{\partial \phi}{\partial z}\right]_i^j = \xi_i^j, \tag{21}$$

$$P_{i+1}^j - P_\infty = \rho \frac{\phi_{i+1}^j - \phi_i^j}{t_{i+1} - t_i}. \tag{22}$$

In the numerical solution of the integral equation (7), the values of ϕ and $\partial\phi/\partial n$ are assumed to vary linearly in the $\theta = 0$ plane as the source point is varied along each panel. The integral equation in its discrete form can be written

$$\alpha^i\phi^i = \sum_{j=1}^{N}\left(G^{1,i,j}\left(\frac{\partial\phi}{\partial n}\right)^j + G^{2,i,j}\left(\frac{\partial\phi}{\partial n}\right)^{j+1}\right) - \sum_{j=1}^{N}(GN^{1,i,j}\phi^j + GN^{2,i,j}\phi^{j+1}), \tag{23}$$

where $N = n_c + n_w$ and

$$G^{1,i,j} = \int_0^{L^j} r(l^j)\frac{L^j - l^j}{L^j}\int_0^{2\pi}\frac{1}{|\boldsymbol{p}^i - \boldsymbol{q}^j(r,\theta)|}\,\mathrm{d}\theta\,\mathrm{d}l^j,$$

$$G^{2,i,j} = \int_0^{L^j} r(l^j)\frac{l^j}{L^j}\int_0^{2\pi}\frac{1}{|\boldsymbol{p}^i - \boldsymbol{q}^j(r,\theta)|}\,\mathrm{d}\theta\,\mathrm{d}l^j,$$

$$GN^{1,i,j} = \int_0^{L^j} r(l^j)\frac{L^j - l^j}{L^j}\int_0^{2\pi}\frac{\partial}{\partial n}\left(\frac{1}{|\boldsymbol{p}^i - \boldsymbol{q}^j(r,\theta)|}\right)\mathrm{d}\theta\,\mathrm{d}l^j,$$

$$GN^{2,i,j} = \int_0^{L^j} r(l^j)\frac{l^j}{L^j}\int_0^{2\pi}\frac{\partial}{\partial n}\left(\frac{1}{|\boldsymbol{p}^i - \boldsymbol{q}^j(r,\theta)|}\right)\mathrm{d}\theta\,\mathrm{d}l^j.$$

In these equations, the length of panel j in the $\theta = 0$ plane is given by L^j, and l^j is the distance coordinate along the panel. The parameter α^i is the solid angle within the fluid subtended by the fluid surface at node i. On the flow–wall interface, which is taken at $z = 0$, a tangent plane to the panelled surface exists at each node and $\alpha_i = 2\pi$ as it would on a continuous surface. However, for the nodes on the cavity surface, there is no tangent plane and $\alpha^i \neq 2\pi$. The integrations in the θ-direction were carried out analytically following the method of Jaswon & Symm (1977); results in terms of elliptic integrals were obtained. The integrations in l^j were carried out numerically using Gauss–Legendre quadrature techniques for the regular parts of the integrals and the quadrature methods of Anderson (1965) for the singular parts of the integrals.

Starting the calculations has turned out to be rather difficult. The problem lies in computing the value of the pressure on the membrane at $t = 0$. From the linearized form of Bernoulli's equation (22), the computation of the pressure on the membrane requires the value of ϕ at the beginning and end of a time step. From the integral equation, $\phi = 0$ on the membrane at $t = 0$ since the values of ϕ on the cavity and $\partial\phi/\partial n$ on the membrane are both zero. In proceeding to time Δt to obtain the required values of ϕ on the membrane, the position of the nodes on the cavity and the corresponding values of ϕ are obtained from (15) or (16). In order to get ϕ on the membrane surface, the value of $\partial\phi/\partial n$ must be known there so that the integral equation (23) can be solved. However, $\partial\phi/\partial n$ is computed from the membrane velocity and this value requires the pressure on the membrane at $t = 0$. Unfortunately, this pressure is the quantity that was being sought in the first place. An iterative scheme was devised to overcome this problem. On the first iteration, the pressure on $z = 0$ at $t = 0$ is computed assuming the coating to be rigid. This allows for the computation of an approximate value of $\partial\phi/\partial n$ on the membrane at $t = \Delta t$. The calculation then proceeds for a few time steps with a relatively stiff compliant boundary. The pressure on the wall soon settles down to a distribution that is nearly constant in time. At this point, the calculation is restarted with the equilibrated pressure distribution and a softer wall. This procedure is repeated until the desired coating properties are achieved. It should be noted that this method can not be used to start the calculation with a growing cavity which will later reach a maximum size and then collapse. The reason for this restriction is that the method requires the pressure distribution on the wall to be nearly constant during the first ten or so time steps of the calculation. If the cavity collapses from rest at its maximum size, the pressure distribution on the wall has this property (see §4). However, if the cavity is initially growing from a small size, the pressure distribution will change rapidly in the initial part of the calculation and the method will not work.

In the calculations described in the following section, the cavity is represented by 32 panels which are of equal arc in the $\theta = 0$ plane at the beginning of the calculation when the cavity is spherical. The number of panels on the flow–wall interface depends on the radius of the compliant coating. The nodes on the part of the boundary containing the coating are spaced at equal intervals of $0.05R_0$ starting at $r = 0$. The length of the panels on the rigid portion of the wall increases linearly from $0.05R_0$ adjacent to the compliant section to a maximum value with the last node at $r = 100R_0$. Fifty panels were used to represent this rigid part of the wall. Thus, for example, in the calculations with $R_m = 2.5R_0$ there were a total of 100 panels on the flow–wall interface (50 on the compliant part of the wall and 50 on the rigid part of the wall). The number and distribution of panels on the cavity and the wall was chosen by performing a set of calculations holding the dimensionless parameters of the problem constant and increasing the number of panels on the cavity and the number and maximum radius of the wall panels until the calculation converged.

The time step of the calculation varied during each run starting with an initial value in most cases of $\Delta t_0 = 0.005T_0$ (where T_0 is defined below) and ending with a value greater than or equal to $\Delta t_{min} = \Delta t_0/200$. At each step, the time difference

$$\Delta t_v = \frac{\Delta \Phi_{max}}{1+0.5q_{max}^2}$$

was computed, where $\Delta\Phi_{max}$ is a constant and q_{max} is the maximum fluid velocity on the surface of the cavity at any time step. If $\Delta t_{min} < \Delta t_v < \Delta t_0$ then Δt_v was used as the time step. If $\Delta t_v > \Delta t_0$ the time step was taken as Δt_0, while if $\Delta t_v < \Delta t_{min}$ the time step was taken as Δt_{min}.

4. Results

There are a number of independent variables in this solid–fluid interaction problem. For the fluid, these variables include the initial radius of the cavity, R_0, the initial distance of the cavity from the wall, Z_0, the pressure difference, $\Delta P = P_\infty - P_0$, and the density of the fluid, ρ. For the coating, the variables are the mass per unit area, m, the tension, T, the spring constant, K, and the radius of the coating, R_m. One of the most interesting parameters describing the collapse of the cavity is z_c, the height above the wall where the north and south poles of the cavity meet at the end of the collapse. Thus, z_c is a function of eight independent variables. In terms of dimensionless variables, we find

$$\frac{z_c}{R_0} = f\left(\frac{Z_0}{R_0}, \frac{R_m}{R_0}, \frac{m}{\rho R_0}, \frac{KR_0}{\Delta P}, \frac{T}{R_0 \Delta P}\right). \tag{24}$$

For ease of reference, we define the last three dimensionless variables on the right-hand side of (24) as M^*, K^*, and T^*, respectively. The first, M^*, is the ratio of the mass per unit area of the membrane to an equivalent mass per unit area of the fluid based on a thickness R_0. The last two, K^* and T^*, are the ratio of the spring and tension terms in the membrane equation to the pressure driving the collapse. The time for the collapse of a cavity in an infinite fluid is $0.915T_0$, where $T_0 = R_0[\rho/(P_\infty - P_0)]^{\frac{1}{2}}$. Thus, the timescale for the flow is taken as T_0. Note that if T_0 is used for the timescale in the membrane equation, M^* is the ratio of the inertial term in the membrane equation to the pressure difference driving the collapse. Other physically interesting dimensionless ratios can be obtained by comparing the timescale of the flow to the timescale of the coating. The timescale for the coating can be obtained by Hankel–Laplace transform techniques applied to (4) in the absence of the flow. From this analysis, one finds that

$$\left(\frac{T_0}{T_{\mathrm{m}}}\right)^2 = \frac{T^*}{M^*}\left(\frac{\lambda_n}{\pi}\right)^2 + \frac{K^*}{M^*}\left(\frac{1}{\pi}\right)^2. \tag{25}$$

where T_{m} is one-half the period of free oscillations for the coating and λ_n ($n = 1, 2, 3, \ldots$) are the zeros of the zeroth-order Bessel function. In most of the calculations presented herein, the value of T^* is quite small so one would expect the spring–mass term, K^*/M^*, to dominate the ratio of the flow timescale to the coating timescale for the lower modes. In the following, all lengths and times are non-dimensionalized by R_0 and T_0 respectively, and the dimensionless time is denoted by t^*.

In performing the calculations, two modes of instability were found. The first occurs if the tension is too large and can be stabilized by reducing the time step. For instance, with $T^* = 0.25$, $Z_0 = 1.5R_0$, $R_{\mathrm{m}} = 3.5R_0$, $M^* = 1.5$ and $K^* = 2.0$ the calculation was stable with an initial time step of 0.005; however, while when T^* was increased to 2.5 while holding the other parameters constant, the time step had to be reduced to 0.0025 to obtain stable results. This instability appeared as an oscillation in the membrane surface with high spatial frequency that starts near $r = R_{\mathrm{m}}$ and spreads inward. It is suspected that this instability is related to the instabilities generally found in the solution to hyperbolic equations like the one describing the coating. The second instability occurs when the mass of the membrane is too low or the membrane radius is too large. For instance, for R_{m} greater than about $3.75R_0$ it was not possible to obtain a stable calculation with M^* low enough to make the collapse spherical. This instability manifested itself as an inability to converge to a stable pressure distribution to start the calculation.

4.1. *The general behaviour of the cavity and the coating*

The cavity profiles, wall pressure profiles and wall velocity profiles at various times during the collapse of a cavity next to four different walls are presented first to give the reader an overview of the phenomenon. The profiles of the cavity at various times for the four cases are presented in figure 3. In all cases, $Z_0 = 1.5R_0$. Figure 3(*a*) depicts the collapse of the cavity next to a rigid wall, while in figures 3(*b*), 3(*c*), and 3(*d*) the wall has a central compliant section with the properties $R_{\mathrm{m}} = 2.5\mathrm{R}_0$ and $T^* = 0.0025$. In all of these latter cases, M^* and K^* are equal, with values of 3.5, 2.0 and 1.0 in figures 3(*b*), 3(*c*) and 3(*d*), respectively. The cavity shapes shown here are typical of all the calculations presented in this paper. In the case of the rigid wall, figure 3(*a*), the typical wall-directed, re-entrant jet can be seen in the profiles near the end of the collapse. The final collapse height, z_{c}, is $1.026R_0$ and the total collapse time, t_{c} (the value of t when the north pole and the south pole of the cavity meet), is $1.033T_0$. This can be compared to $z_{\mathrm{c}} = 1.5R_0$ and $t_{\mathrm{c}} = 0.915T_0$ for a cavity collapsing spherically in an infinite fluid. It should be noted that z_{c} and t_{c} were obtained by

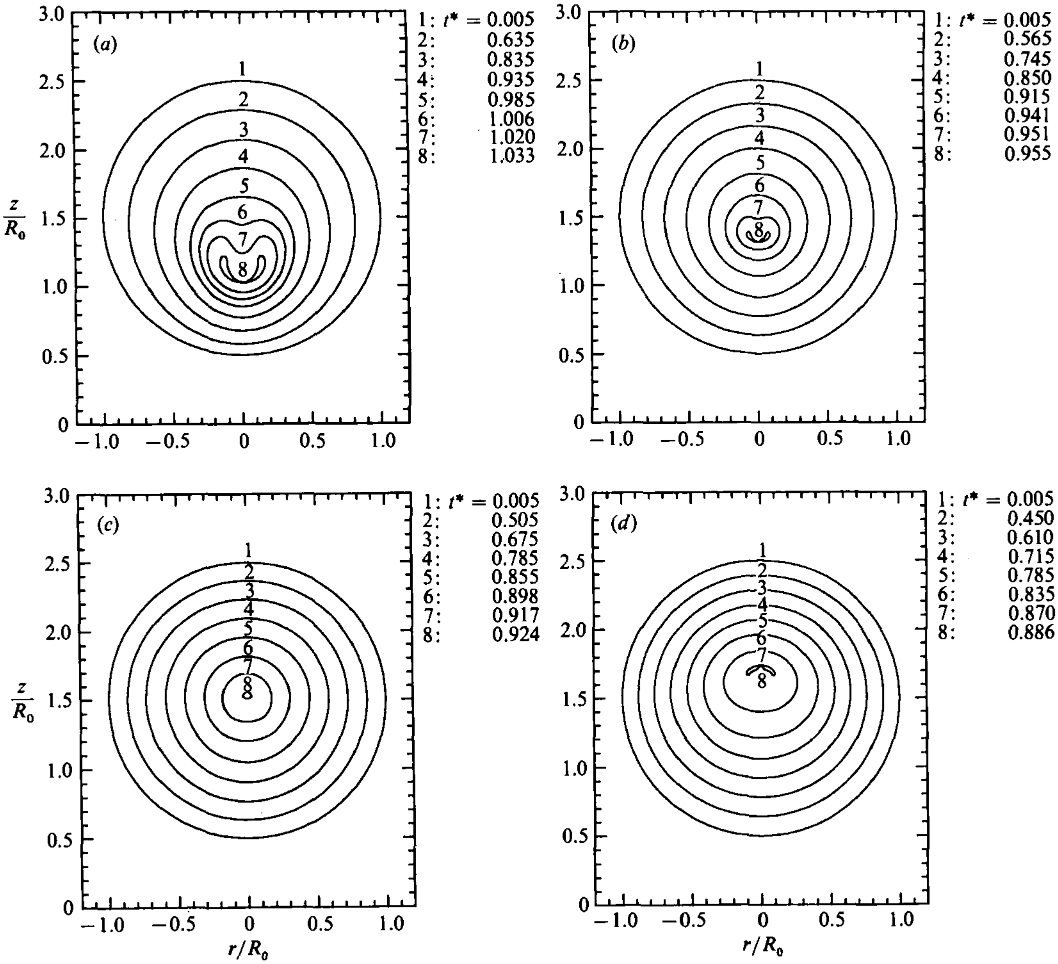

FIGURE 3. Cavity profiles at various times for four cases with $Z_0 = 1.5R_0$: (*a*) Rigid wall; (*b*) $M^* = 3.5$, $K^* = 3.5$, $T^* = 0.0025$, $R_m = 2.5R_0$; (*c*) $M^* = 2.0$, $K^* = 2.0$, $T^* = 0.0025$, $R_m = 2.5R_0$; (*d*) $M^* = 1.0$, $K^* = 1.0$, $T^* = 0.0025$, $R_m = 2.5R_0$.

linear extrapolation from the point in the collapse where the north and south poles were about $0.006R_0$ apart. This extrapolation is necessary since the calculation of the Green's functions becomes inaccurate when the upper panels get too close to the lower panels. For the case with $M^* = K^* = 3.5$ (figure 3*b*), the interaction with the relatively stiff compliant wall has modified the collapse so that the collapse height, $z_c = 1.311R_0$, and collapse time, $t_c = 0.955T_0$, are closer to the values for a spherical collapse in an infinite fluid. When M^* and K^* are reduced to 2.0 (figure 3*c*), all the cavity profiles are nearly spherical and the values of z_c and t_c ($1.552R_0$ and $0.924T_0$, respectively) are very close to their values for the collapse of a cavity in an infinite fluid. It should be noted that in cases of nearly spherical collapse, the calculation becomes unstable near the end of the collapse so z_c and t_c are a little more speculative than in the other calculations. The profiles shown in figure 3(*d*) are for $M^* = K^* = 1.0$. In this case, the jet can be seen directed away from the wall in the final stages of the collapse with $z_c = 1.740R_0$ and $t_c = 0.886T_0$.

The distributions of the pressure $(P_m - P_\infty)$ on the wall during the collapse corresponding to figure 3(*a–d*) are shown in figure 4(*a–d*), respectively. The time of

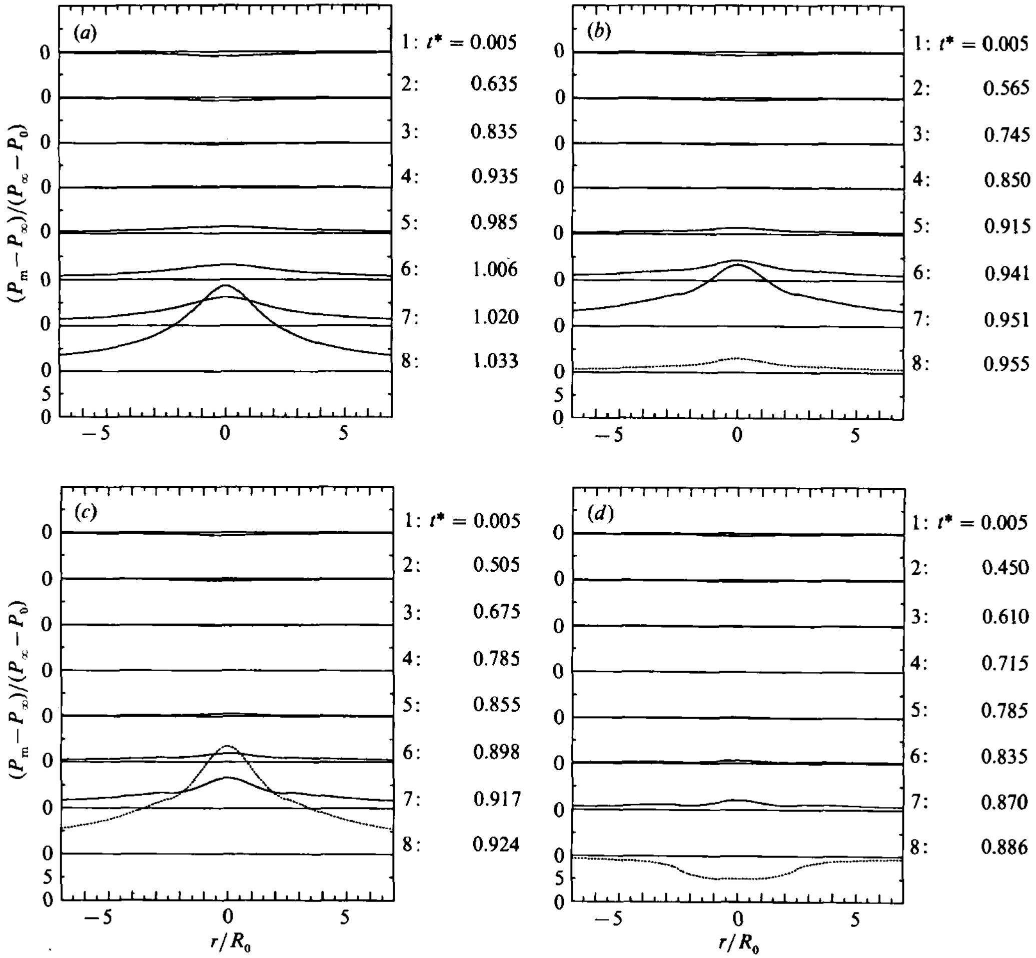

FIGURE 4. Pressure profiles on the wall at times and conditions corresponding to figure 3. In (*b*), (*c*) and (*d*) the values of curve 8 have been divided by 20.

each distribution corresponds to the time of each profile in figure 3. (Note that in distributions number 8 for figures 4(*b*), 4(*c*) and 4(*d*), the pressures have been divided by a factor of 20.) In each distribution, the pressure is a maximum at $r = 0$ and tends to zero as r tends to infinity. In the compliant-wall cases, there are wiggles in the pressure distributions near the boundary between the rigid and compliant parts of the wall. The pressure at $r = 0$ starts with a value ranging from $-0.922\Delta P$ for the rigid wall (figure 4*a*) to $-0.565\Delta P$ for the most compliant wall (figure 4*d*). Toward the end of the collapse, this pressure becomes positive and has a much larger magnitude in figure 4(*a*–*c*). However, in figure 4(*d*), the case in which the re-entrant jet is directed away from the wall, the pressures at the end of the collapse are negative. It is dangerous to make detailed comparisons of the magnitudes of the pressure profiles in figure 4 at the end of the collapse from one case to another because the pressure is changing very rapidly at this time. This comparison will be addressed later by plotting the pressure in a different manner.

The vertical velocity profiles on the wall corresponding to the four cases shown in figure 3 are presented in figure 5. The vertical velocity on the rigid part of the

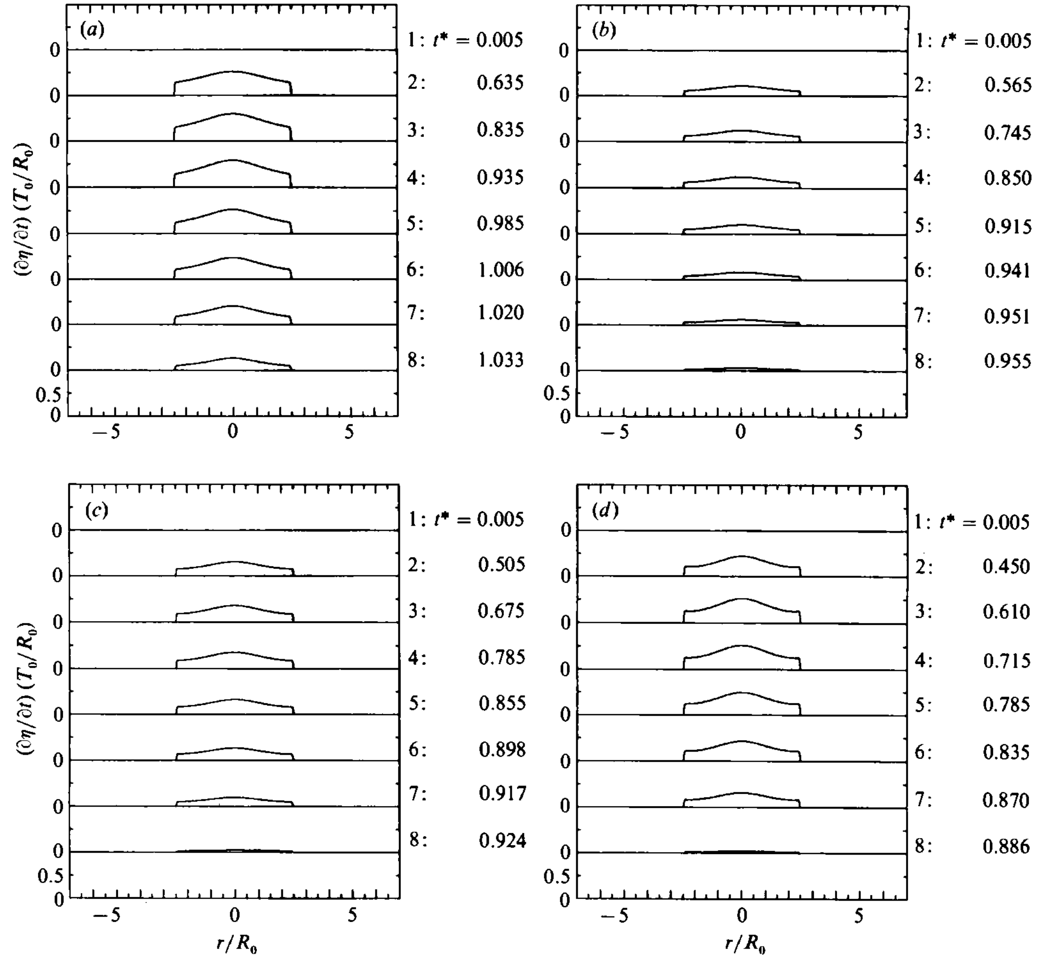

FIGURE 5. Vertical velocity profiles on the wall at times and conditions corresponding to figure 3; (*a*) is a one-way interaction.

boundary is, of course, zero. In figure 5(*a*), the pressure from the rigid-wall calculation was used to drive a compliant wall with the same properties as the one in figure 5(*c*). This was a one-way interaction; the motion of the wall did not affect the collapse of the cavity. The velocity distributions in the four cases are similar. At times early in the collapse, the distributions are all positive since the pressures are negative. A maximum can be seen at $r = 0$ and near the outer edge of the compliant wall the velocity decreases to zero rapidly. At later times, the velocity decreases in magnitude. From figure 5(*b*–*d*), it can be seen that the velocities generally increase with the softness of the coating (decreasing M^* and K^*). The largest velocities occur during the one-way interaction case in figure 5(*a*).

4.2. *The effect of M^* and K^**

Let us now consider the effect of M^* and K^* as they are varied independently with fixed $T^* = 0.0025$, $Z_0 = 1.5R_0$ and $R_m = 2.5R_0$. Figure 6 contains plots of the height of the north pole and south pole of the cavity versus time. There are three plots, each with a set of calculations with the same value of K^*: 0.25, 2.0 and 8.0 in figure 6(*a*), 6(*b*) and 6(*c*), respectively. Each curve is for a different value of M^* and these values

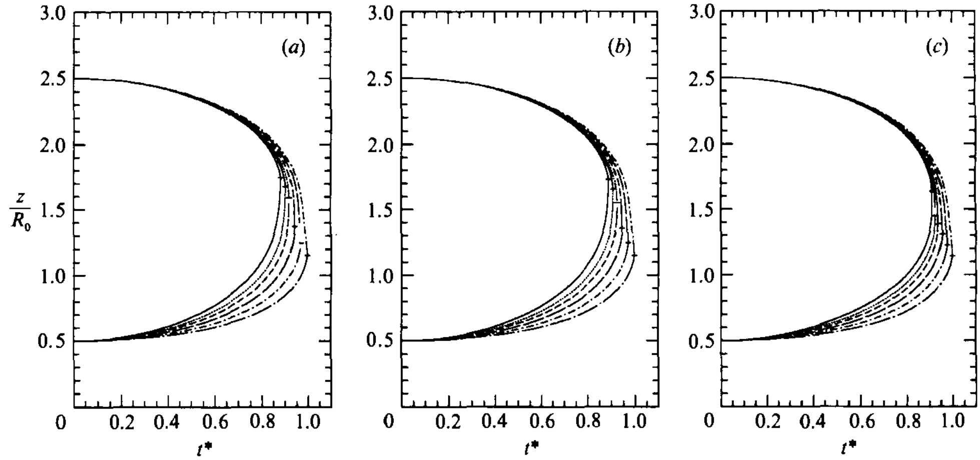

FIGURE 6. Height of the north and south poles of the cavity versus time. $Z_0 = 1.5R_0$, $R_m = 2.5R_0$, $T^* = 0.0025$: (*a*) $K^* = 0.25$; (*b*) $K^* = 2.0$; (*c*) $K^* = 8.0$. $M^* = 1.0$ (——), $M^* = 1.5$ (·····), $M^* = 2.0$ (------), $M^* = 3.0$ (——), $M^* = 5.0$ (–·–·–), $M^* = 10.0$ (·—·—).

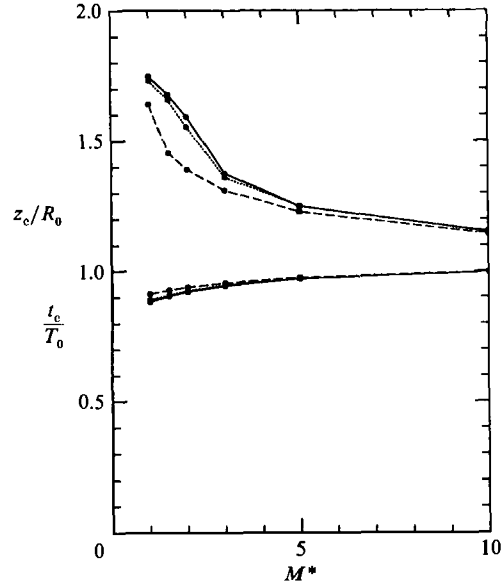

FIGURE 7. Collapse height, z_c/R_0, (upper curves) and collapse time, t_c/T_0, (lower curves) versus M^* for $Z_0 = 1.5R_0$, $R_m = 2.5R_0$ and $T^* = 0.0025$. $K^* = 0.25$ (——), $K^* = 2.0$ (·····), $K^* = 8.0$ (------).

are the same in each figure: 1.0, 1.5, 2.0, 3.0, 5.0 and 10.0. The short horizontal lines at the end of each collapse indicate the projected values of z_c. Note that for each value of K^*, as M^* is reduced (i.e. as the inertia of the membrane is reduced relative to $R_0\rho$) the collapse becomes nearly spherical, $z_c \approx Z_0$, and then for even smaller values of M^*, $z_c > Z_0$ indicating that the re-entrant jet is directed away from the wall. Thus, it appears that it is possible, given a wall with sufficiently low mass, to redirect the re-entrant jet over a wide range of values of the spring constant. To summarize these data, a plot of z_c and t_c versus M^* for the three values of K^* from figure 6 is given in figure 7. In all cases, the collapse height increases and the collapse time decreases with decreasing M^*. The value of M^* required to cause a spherical

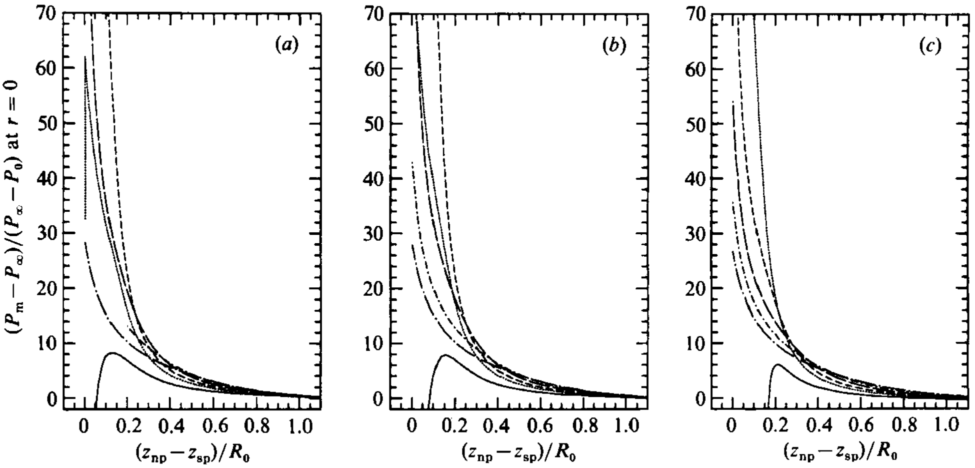

FIGURE 8. Pressure on the membrane surface at $r = 0$ versus vertical separation between the north and south poles of the cavity. $Z_0 = 1.5R_0$, $R_m = 2.5R_0$, $T^* = 0.0025$: (a) $K^* = 0.25$; (b) $K^* = 2.0$; (c) $K^* = 8.0$. $M^* = 1.0$ (——), $M^* = 1.5$ (·····), $M^* = 2.0$ (– – – – –), $M^* = 3.0$ (— — —), $M^* = 5.0$ (–·–·–·–), $M^* = 10.0$ (·—·—).

collapse, $z_c = 1.5R_0$, decreases as K^* is increased. It is interesting to examine the timescale ratio, T_m/T_0, from (25) when the collapse is spherical for the three values of K^*. The required values of M^* were obtained from linear interpolation of the curve of collapse height versus M^* for each of the three cases. For the lowest mode ($\lambda_1 = 2.405$), the term in (25) involving T^* is very small relative to the spring–mass term. Thus, using $T_m/T_0 = \pi(M^*/K^*)^{\frac{1}{2}}$, we find $T_m/T_0 = 9.77$, 3.34 and 1.32 for $K^* = 0.25$, 2.0 and 8.0, respectively, From these data, it appears that spherical collapse can occur for a fairly wide range of the timescale ratio. This indicates that the ratio of the timescales does not dominate the physics of the interaction. The values of t_c for spherical collapse were $0.930T_0$, $0.930T_0$ and $0.923T_0$ for $K^* = 0.25$, 2.0 and 8.0, respectively. These collapse times are fairly close to the time for collapse in an infinite fluid, $0.915T_0$.

The pressures on the compliant wall directly under the south pole of the cavity, $r = 0$, are shown in figure 8(a–c) for the set of collapses from figure 6. At the end of the collapse, the pressure increases very rapidly so it was found convenient to plot the pressure versus the distance between the north and south poles of the cavity. This expands the horizontal scale on the plots toward the end of the collapse and creates a basis to compare the pressures at similar stages during the process. For all the cases shown, the pressure is initially constant with a value greater than $-1.0\Delta P$. For the membranes with larger M^*, the pressure on the wall then rises slowly, and finally rises rapidly at the end of the collapse. This rapid pressure increase occurs at a larger value of the distance between the poles as the value of M^* is decreased. When the collapse is nearly spherical, the rapid pressure rise occurs at the largest separation of the poles. The pressure profile shows a dramatic change when M^* is small enough to produce a collapse directed away from the wall: toward the end of the collapse (at pole separations that are less than those at the rapid pressure rise in the spherical cases) the pressure reaches a maximum and then decreases rapidly. The maximum positive pressure during the collapse is hard to measure in the cases where it is increasing rapidly toward the end. However, it can be said that as the wall becomes softer, this maximum pressure first increases, probably reaching a maximum value when the collapse is spherical.

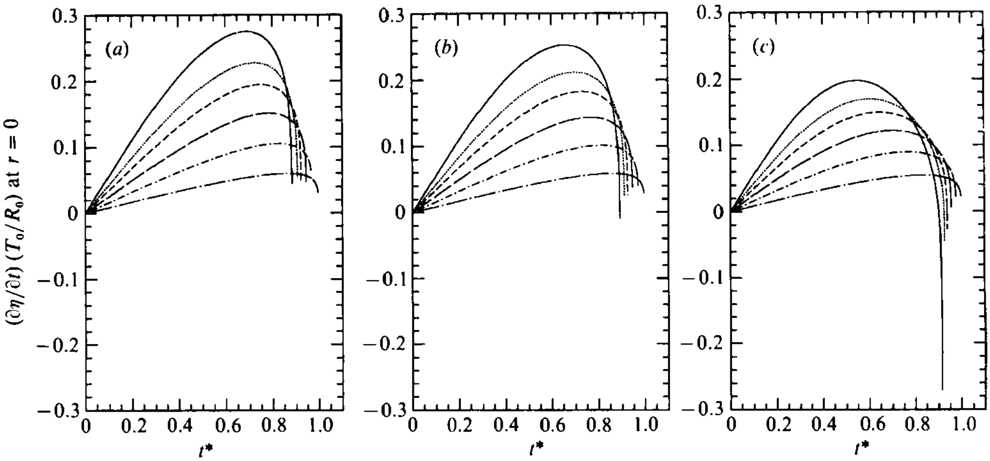

FIGURE 9. Vertical velocity of the membrane at $r = 0$ versus time. $Z_0 = 1.5R_0$, $R_m = 2.5R_0$, $T^* = 0.0025$: (a) $K^* = 0.25$; (b) $K^* = 2.0$; (c) $K^* = 8.0$. $M^* = 1.0$ (——), $M^* = 1.5$ (·····), $M^* = 2.0$ (– – – – –), $M^* = 3.0$ (——), $M^* = 5.0$ (–·–·–·–), $M^* = 10.0$ (·—·—).

In figure 9, the vertical velocity of the membrane at the position $r = 0$ is plotted versus time for the same conditions as in figure 6. In all cases, the velocity reaches a positive peak somewhere in the latter half of the collapse and then decreases toward the end of the collapse, in some cases finally becoming negative. The time at which the maximum velocity occurs decreases with decreasing M^* for all three values of K^*. For $K^* = 2.0$, the time for the maximum velocity varies from $0.8T_0$ at $M^* = 10.0$ to $0.65T_0$ at $M^* = 1.0$. Thus, the time of the maximum velocity has decreased by a factor of 0.81, while T_m/T_0 has decreased by a factor of 0.316. Similar results can be obtained for $K^* = 0.25$ and 8.0. Thus, the effect of the timescale ratio is not as strong as one might have expected initially.

The vertical displacement of the membrane at $r = 0$ can, of course, be obtained from the integral of the curves in figure 9. By examining figure 9, one can deduce that the curves of displacement will increase during most of the collapse and then level off or in a few cases start to decrease just before the end of the collapse. For $M^* = 1.0$, the maximum displacements are $0.162R_0$, $0.153R_0$ and $0.122R_0$ for $K^* = 0.25$, 2.0 and 8.0, respectively.

The physics of the interaction can be examined a little more closely by considering the balance of the terms in the membrane equation during the collapse. Figure 10(*a–c*) contains plots of the inertia term and the spring term in the membrane equation versus time for the cases with $M^* = 1.0$ in figure 6(*a–c*), respectively. The tension term is not plotted since the low value of $T^* (= 0.0025)$ renders it insignificant. In all three cases, the re-entrant jet is directed away from the wall. The three plots are qualitatively similar. At early times, the inertia term is larger than the spring term since the displacements are small. Somewhere toward the middle of the collapse the two terms are about equal. Finally, toward the end of the collapse the inertia term decreases rapidly and reaches large negative values, while the spring term is relatively constant with a value about equal to the initial value of the inertia term. Thus, over most of the collapse the inertia term dominates the spring term in the membrane response equation. The values of M^* when the collapse is nearly spherical are 2.42, 2.25 and 1.41 for $K^* = 0.25$, 2.0 and 8.0, respectively. The rather small variation in M^* compared to the variation in K^* is a reflection of the dominance of the inertia term in the interaction.

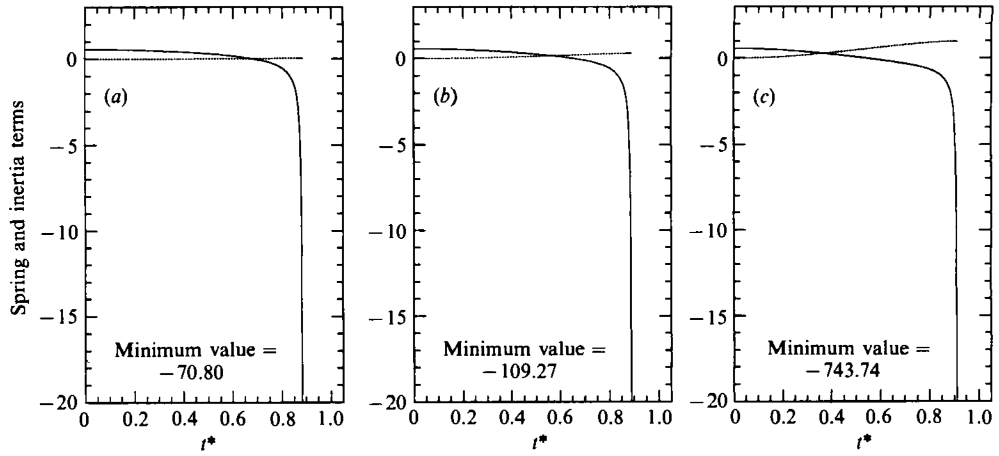

FIGURE 10. Inertia (——) and spring (·····) terms from equation (4) versus time. $Z_0 = 1.5R_0$, $R_m = 2.5R_0$, $M^* = 1.0$, $T^* = 0.0025$: (*a*) $K^* = 0.25$; (*b*) $K^* = 2.0$, (*c*) $K^* = 8.0$.

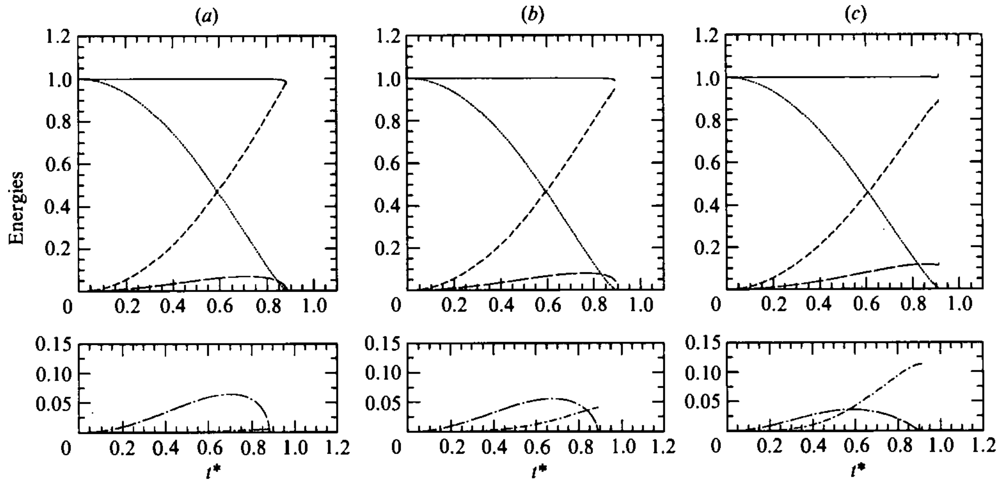

FIGURE 11. Energies of the flow and the coating versus time. $Z_0 = 1.5R_0$, $R_m = 2.5R_0$, $M^* = 1.0$, $T^* = 0.0025$: (*a*) $K^* = 0.25$, (*b*) $K^* = 2.0$, (*c*) $K^* = 8.0$. Sum of all energies ——, KEF (– – – – – –), PEF (·····), KEM (—·—·), PES (·–·–·–·–), PW (———).

Plots of the kinetic (KEF) and potential (PEF) energies of the flow, the kinetic energy of the membrane (KEM), the potential energy of the spring (PES) and the work done at the flow–coating boundary (PW) are plotted versus time in figure 11 (*a–c*) for the three cases from figure 10 (*a–c*), respectively. Each plot consists of two parts: in the upper part the flow energies, the pressure work and the sum of the three are shown; in the lower part, on an expanded scale, the two energies of the coating are shown. The total energy of the calculation should remain constant and was found never to vary by more than 0.5%. In all cases, the system starts with PEF = 1.0 and values of zero for all the other energies. As the collapse proceeds, PEF drops while KEF and the total energy in the coating increase. The total energy in the coating is never more than about 10% of the total energy of the flow–coating system. For the case with $K^* = 0.25$, the energy in the coating is almost all in the kinetic energy. In the case with $K^* = 2.0$, the coating energy is also dominated by the kinetic energy

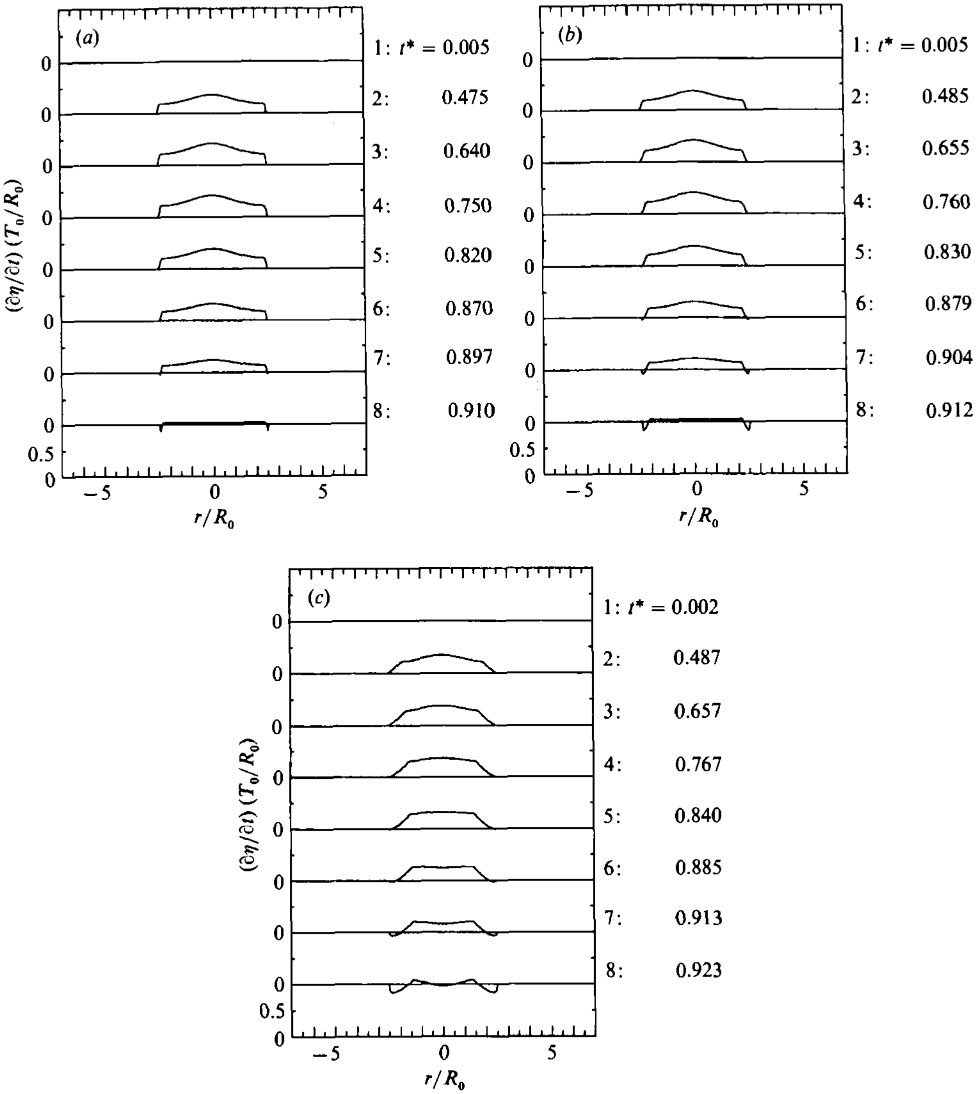

FIGURE 12. Distributions of vertical velocity on the wall at various times for $Z_0 = 1.5R_0$, $R_m = 2.5R_0$, $M^* = 1.5$ and $K^* = 2.0$. (*a*) $T^* = 0.025$, (*b*) $T^* = 0.25$ and (*c*) $T^* = 2.5$.

term but the energy in the spring is visible in the plot. In the case with $K^* = 8.0$, the coating energy is dominated by the spring during the last half of the collapse.

4.3. *The effect of* T^*

In all of the results presented previously, the small value of the membrane tension, $T^* = 0.0025$, has rendered the influence of this effect negligible. In order to explore the influence of the membrane tension, a set of calculations were performed with $Z_0 = 1.5R_0$, $M^* = 1.5$, $K^* = 2.0$, $R_m = 2.5R_0$ and three values of T^*: 0.025, 0.25 and 2.5. The profiles of the cavity versus time are very similar and therefore are not shown here. The collapse heights were $1.656R_0$, $1.652R_0$ and $1.622R_0$ for $T^* = 0.025$, 0.25 and 2.5, respectively. The distributions of vertical velocity on the wall at various times during the collapse are shown in figure 12 for the three values of T^*. The most prominent effect of the tension is in the region near the outer edge of the compliant

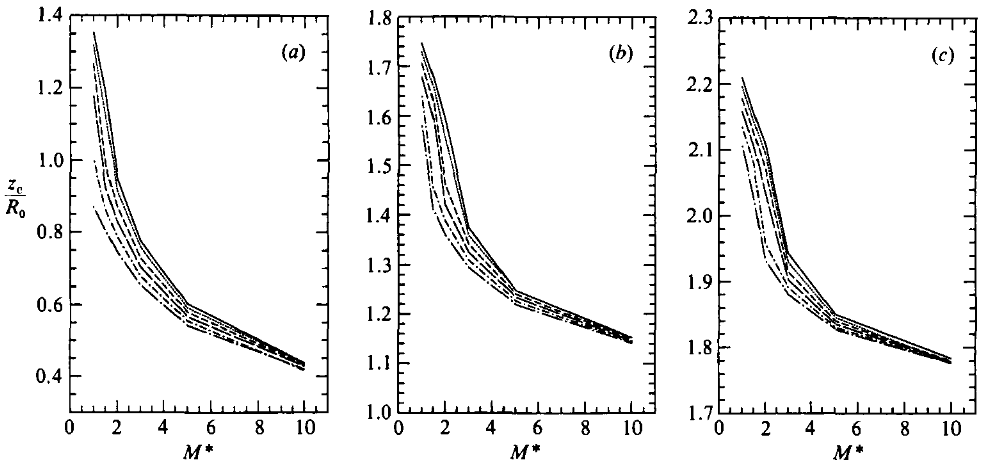

FIGURE 13. Collapse height, z_c/R_0, versus M^*. $R_m = 2.5R_0$, $T^* = 0.0025$: (*a*) $Z_0/R_0 = 1.1$, (*b*) $Z_0/R_0 = 1.5$, (*c*) $Z_0/R_0 = 2.0$. $K^* = 0.25$ (——), $K^* = 2.0$ (·····), $K^* = 4.0$ (– – – – – –), $K^* = 6.0$ (——), $K^* = 8.0$ (–·–·–·–), $K^* = 10.0$ (–·——·–).

surface. When the tension is very small (see figure 5), the velocity of the membrane is nearly constant near the edge of membrane and suddenly drops to zero at $r = R_m$. When the tension is larger, regions of negative velocity near the edge of the coating develop toward the end of the collapse. The width of these regions increases as the tension is increased. This is consistent with the higher resistance to membrane curvature in the calculations with higher tension. It is emphasized, however, that in the range of parameters used herein, the tension played a much less dramatic role than M^* and K^* in controlling the dynamics of the cavity–coating interaction.

4.4. *The effect of the initial height of the cavity and the radius of the coating*

The geometrical aspects of the problem are described by the ratio of the initial height of the centre of the cavity to its initial radius, Z_0/R_0, and the ratio of the radius of the coating to the initial radius of the cavity, R_m/R_0. The effect of Z_0/R_0 on the cavity–coating interaction is summarized by the plots of collapse height versus M^* in figure 13. Three plots are shown for $Z_0/R_0 = 1.1$, 1.5 and 2.0 in figure 13(*a–c*), respectively. In each plot, curves are given for six values of K^*. The qualitative behaviour of all the curves is the same: as M^* is decreased the collapse height increases. Since the minimum value of z_c occurs for a rigid wall, it appears that, for a given M^*, the higher the value of K^*, the closer the collapse is to the rigid-wall case. To further reduce the data, the curves in figure 13 were interpolated linearly to obtain curves of $z_c = Z_0$ on a plot of M^* versus K^* for each value of Z_0, figure 14. The curves look a little scattered owing to the previously mentioned instabilities when the collapse is nearly spherical. For each curve, the re-entrant jet is directed toward the wall if the values of M^* and K^* are outside the curve and away from the wall if the values are inside the curve. For a given K^*, the closer the cavity is to the wall, the lower the value of M^* that is needed for a spherical collapse.

The effect of the coating radius on the collapse is illustrated by figure 15 which is a plot of z_c versus M^* for fixed $Z_0 = 1.5R_0$, $K^* = 2.0$ and $T^* = 0.0025$ and three different values of R_m/R_0 (1.25, 2.5 and 3.75). The results for $R_m = 2.5R_0$ and $R_m = 3.75R_0$ are nearly identical, indicating that beyond a diameter of $2.5R_0$, the radius of the coating has little effect on the results. This is to be expected since the influence of the wall motion on the cavity must die out with distance from the cavity.

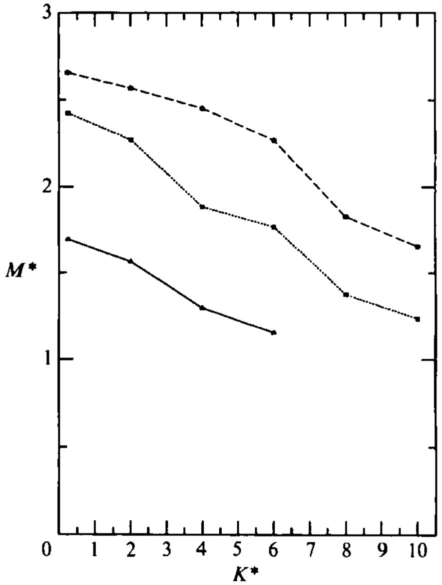

FIGURE 14. Contours of $z_c/R_0 = Z_0/R_0$ on a plot of M^* versus K^*. $T^* = 0.0025$, $R_m = 2.5R_0$: $z_0 = 1.1R_0$ (——), $z_0 = 1.5R_0$ (·····), $z_0 = 2.0R_0$ (– – – – – –).

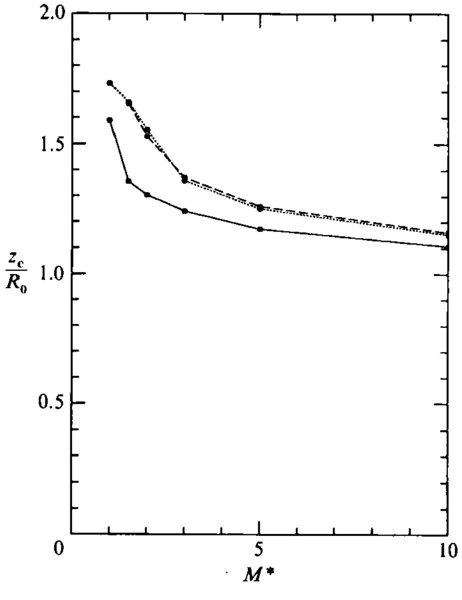

FIGURE 15. Collapse height, z_c, versus M^* with $K^* = 2.0$, $T^* = 0.0025$ and $Z_0 = 1.5R_0$. $R_m = 1.25R_0$ (——), $R_m = 2.5R_0$ (·····), $R_m = 3.75R_0$ (– – – – –).

4.5. *Comparison with published experimental data*

The only extensive set of experimental data on the behaviour of cavities near compliant walls is that published by Shima *et al.* (1989). Unfortunately, there are several differences between the present calculations and the conditions of these experiments that prevent a valid comparison. Probably the most important difference is that in the experiments the cavity is spark generated and so grows and

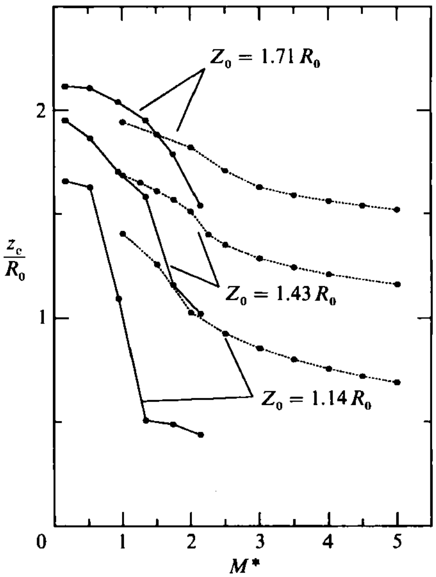

FIGURE 16. Comparison of the experimental data from Shima *et al.* (1989) (——), which is for a cavity that expands and then collapses, with results from the present calculations (·····), which are for a cavity which collapses from rest. In the experiments the coating has an unknown bending stiffness while in the calculations the bending stiffness is zero. Plot of z_c versus M^* with $K^* = 0.088$, $T^* = 0$, $R_m = 2.5R_0$.

then collapses, while in the calculations the cavity collapses from rest when it is at its maximum size. As is explained in §3, this restriction on the numerical model is necessitated by the method used to start the calculation. The difference in the results between the two cases can be quite important. For example, if the cavity collapses from rest next to a rigid wall with $Z_0 = 1.5R_0$, we find $z_c = 1.026R_0$, while if the cavity grows and then collapses from the same initial height and an initial radius of 10% of its maximum size, we find $z_c = 0.798R_0$. Another difference between the experiments and the present calculations concerns the construction of the coating. The coating used by Shima *et al.* consisted of an untensioned layer of rubber backed by a layer of foam. The rubber layer had finite thickness and so a finite bending stiffness, while in the numerical model there was no bending stiffness. From Shima *et al.* (1989), the properties of this outer layer are $E = 95.6$ kPa and a maximum thickness $h = 5.0$ mm. Thus, if we assume that the material is incompressible, the maximum bending stiffness ($B_{\max}$) is

$$B_{\max} = \tfrac{1}{12}Eh^3_{\max} = 0.001\,\mathrm{Nt\,m}$$

(Landau & Lifshitz 1986). To include bending effects in the membrane equation one would have to add a term $B\nabla^4\eta$ (where ∇ is the gradient operator for the membrane in cylindrical coordinates) to the membrane equation (4). After non-dimensionalizing η and r with R_0 and dividing by ΔP, the dimensionless bending stiffness can be found which is directly comparable to M^*, K^* and T^*:

$$B^*_{\max} = \frac{B_{\max}}{R_0^3\Delta P} = 0.23.$$

Thus, if the value of E given in Shima *et al.* (1989) is correct, one might guess that this relatively small bending stiffness would not have a large effect. Unfortunately, the value of E is probably not reliable since it appears to have been measured statically and the modulus of rubber-like materials is highly frequency dependent (Hunston, Yu & Bullman 1984). The static value is likely to be much too low. Thus, it is not possible to accurately assess the magnitude of the neglected bending stiffness in the present model. Another difference between the calculations and the experiments is that the coating in the experiments was surrounded by a free surface rather than a rigid wall as in the calculations. In the experiments $R_m/R_0 = 5.7$. Owing to the instabilities in the calculation procedure, it was not possible to perform calculations with low values of M^* and this large value of R_m. However, given the results in the previous section showing that increases in the coating radius over $2.5R_0$ do not effect the results very much, it is not expected that the free surface or the larger coating radius in the experiments would cause a major change in the results.

In spite of these problems, a comparison of the present numerical results with the experimental results of Shima *et al.* (1989) is presented in figure 16. The experimental data is from their figure 10 and is a plot of z_c versus M^*. (Owing to differing definitions, the dimensionless mass and spring constants used by Shima *et al.* must be divided by π and $\pi R_m^2/R_0^2$ to obtain M^* and K^*, respectively). In the present calculation, $R_m = 2.5R_0$, $T^* = 0$ and $K^* = 0.088$ (a value taken from their paper). Note that the shape of the curves is about the same, but that the calculations are shifted to higher M^* and z_c/R_0. The shift in z_c/R_0 in figure 16 is about equal to the shift in z_c mentioned above when comparing the cases of cavity growth followed by collapse and cavity collapse only for a rigid wall. The magnitude of the shift in M^* is about 1.0.

5. Conclusion

A numerical method for the computation of the collapse of a cavity adjacent to a compliant wall has been presented. When the wall is rigid, the collapse is characterized by the formation of a re-entrant jet that is directed toward the wall. When the wall is compliant, it is possible to create a spherical collapse or to direct the re-entrant jet away from the wall for a fairly wide range of wall parameters. This drastic change in behaviour of the cavity occurs when the displacements in the coating are about 15% of the initial cavity radius and when the total energy transferred to the coating from the flow is about 10% of the total flow–coating energy. When the parameters are such that the collapse is spherical, the value of T_0/T_m (the ratio of the timescale for the collapse of a cavity in an infinite fluid to the spring–mass timescale for the membrane) is found to vary widely, indicating that this ratio does not dominate the physics of the interaction. In the range of coating parameters studied herein, the interaction is most sensitive to M^* $(= m/(\rho R_0)$, where m is the mass per unit area of the membrane, ρ is the density of the fluid and R_0 is the initial radius of the cavity).

This work was begun while J. H. Duncan was at Flow Research Company and was supported by the Office of Naval Research under contract N00014-85-C-0747. The authors wish to acknowledge Georges Chahine for a number of helpful discussions and for suggesting the problem and Ugo Piomelli for several discussions concerning the numerical aspects of the problem. The support of the San Diego Supercomputer Center where some of the calculations were performed is also gratefully acknowledged.

REFERENCES

ANDERSON, D. G. 1965 Gaussian quadrature formulae for $-\int_0^1 \ln(x) f(x)\,dx$. *Maths Comput.* **19**, 477–481.

BLAKE, J. R. & GIBSON, D. C. 1981 Growth and collapse of a vapour cavity near a free surface. *J. Fluid Mech.* **111**, 123–140.

BLAKE, J. R. & GIBSON, D. C. 1987 Cavitation bubbles near boundaries. *Ann. Rev. Fluid Mech.* **19**, 99–123.

BLAKE, J. R., TAIB, B. B. & DOHERTY, G. 1986 Transient cavities near boundaries. Part 1. Rigid boundary. *J. Fluid Mech.* **170**, 479–497.

BLAKE, J. R., TAIB, B. B. & DOHERTY, G. 1987 Transient cavities near boundaries. Part 2. Free surface. *J. Fluid Mech.* **181**, 197–212.

CHAHINE, G. L. 1977 Interaction between an oscillating bubble and a free surface. *Trans. ASME* I: *J. Fluids Engng* **99**, 709–715.

CHAHINE, G. L. & BOVIS, A. G. 1983 Pressure field generated by nonspherical bubble collapse. *Trans. ASME* I: *J. Fluids Engng* **105**, 356–363.

DOMMERMUTH, D. G. & YUE, D. K. P. 1987 Numerical simulations of nonlinear axisymmetric flows with a free surface. *J. Fluid Mech.* **178**, 195–210.

FERZIGER, J. H. 1981 *Numerical Methods for Engineering Application.* John Wiley and Sons.

GIBSON, D. C. & BLAKE, J. R. 1982 The growth and collapse of bubbles near deformable surfaces. *Appl. Sci. Res.* **38**, 215–224.

HUNSTON, D. L., YU, C. & BULLMAN, G. W. 1984 Mechanical properties of compliant coating materials. In *Laminar Turbulent Boundary Layers* (ed. E. M. Uram & H. E. Weber), pp. 85–89. ASME.

JASWON, M. A. & SYMM, G. T. 1977 *Integral Equation Methods in Potential Theory and Elastostatics.* Academic.

LAMB, H. 1945 *Hydrodynamics.* Dover.

LANDAU, L. D. & LIFSHITZ, E. M. 1986 *Theory of Elasticity.* Pergamon.

LICHTMAN, J. Z. 1967 Cavitation erosion performance and related properties of cured sheet elastomeric coating systems. *J. Mater.* **2**, 638–660.

PLESSET, M. S. & CHAPMAN, R. B. 1970 Collapse of initially spherical vapour cavity in the neighbourhood of solid boundary. *J. Fluid Mech.* **47**, 283–290.

RHEINGANS, W. J. 1950 Accelerated cavitation research. *Trans. ASME* **72**, 705–719.

SHIMA, A., TOMITA, Y., GIBSON, D. C. & BLAKE, J. R. 1989 The growth and collapse of cavitation bubbles near composite surfaces. *J. Fluid Mech.* **203**, 199–214.

TOMITA, Y. & SHIMA, A. 1986 Mechanisms of impulsive pressure generation and damage pit formation by bubble collapse. *J. Fluid Mech.* **169**, 535–564.

VOGEL, A., LAUTERBORN, W. & TIMM, R. 1989 Optical and acoustic investigations of the dynamics of laser-produced cavitation bubbles near a solid boundary. *J. Fluid Mech.* **206**, 299–338.